Ultrasensitive Broadband Infrared 4 × 4 Mueller-Matrix Ellipsometry For Studies of Depolarizing and Anisotropic Thin Films

Andreas Furchner,[1] Christoph Kratz,[1] Wojciech Ogieglo,[2] Ingo Pinnau,[2] Jörg Rappich,[3] and Karsten Hinrichs[1]
[1)] *Leibniz-Institut für Analytische Wissenschaften – ISAS – e. V., Schwarzschildstraße 8, 12489 Berlin, Germany*[a)]
[2)] *Functional Polymer Membranes Group, Advanced Membranes and Porous Materials Center, King Abdullah University of Science and Technology (KAUST), Thuwal 23955, Kingdom of Saudi Arabia*
[3)] *Helmholtz-Zentrum Berlin für Materialien und Energie GmbH, Institut für Silizium-Photovoltaik, Kekuléstraße 5, 12489 Berlin, Germany*

(Dated: 22 November 2019)

We present a second-generation broadband 4×4 Mueller-matrix (MM) ellipsometer for ultrasensitive infrared-spectroscopic (8000–800 cm^{-1}) studies of complex nm-thin films. In a modular design, the instrument employs retractable achromatic retarders and various sets of tandem polarizers. Using high-transmittance free-standing wire-grid polarizers, the device reaches an unparalleled precision of up to $5 \cdot 10^{-5}$ in the important fingerprint region, even for block-offdiagonal MM elements. Broadband and signal-to-noise optimized access to the full 4×4 MM provides in-depth information on the sample's polarimetric properties and opens the door for detailed explorations of depolarizing and anisotropic materials. We discuss examples of highly depolarizing non-uniform polyimide membranes, uniaxial-to-biaxial anisotropy changes in ultrathin polymer films, and azimuthal off-axis effects in 2D-structured silica arrays. Diverse optical modeling approaches based upon anisotropic layer stacks and rigorous coupled-wave analysis (RCWA) are used to quantify the optical, structural, and chemical sample properties.

I. INTRODUCTION

Ellipsometry is a well-established, nondestructive and noninvasive linear-optical spectroscopic technique for characterizing the properties of materials by means of polarized light.[1–4] Ellipsometry based upon the Jones formalism addresses non-depolarizing samples. It measures ellipsometric ratios typically expressed as

$$\rho = \tan\Psi \cdot e^{i\Delta} = r_p / r_s, \tag{1}$$

with $\tan\Psi$ and Δ being the amplitude ratio and phase difference between the complex *p*- and *s*-polarized reflection (or transmission) coefficients. Depolarization can be measured using optical retarders and is fully handled by Mueller-matrix (MM) ellipsometry. The 4×4 Mueller matrix obtained by this extended method is a general and complete description of the sample's polarimetric properties.[5]

In recent years, MM ellipsometry has gained much attention as an advanced characterization technique in science and metrology.[6–16] For various reasons, usually related to insufficient signal-to-noise (S/N), the infrared (IR) range is often neglected for thin-film sample analysis. Yet, this spectral region offers detailed complementary insights into optical, physical and chemical sample properties.

Investigating the IR optical response is of particular relevance for organic thin films, which exhibit characteristic vibrational bands due to material-specific absorption, rendering IR spectroscopy a powerful tool for chemical analysis. The IR response is also of interest for studying inorganic layers and structured surfaces, as it delivers information on phonon modes, free charge carriers, structure, and related properties. IR MM ellipsometry, which can measure both amplitude ratios, phase differences and depolarization, has thus become an emerging technique for probing the sample's dielectric properties, its structure and composition, as well as numerous other characteristics, such as optical anisotropy, molecular orientation and interactions.

IR MM measurements are challenging when aiming for thin-film sensitivity. The reasons for this are manifold. Experimental limitations arise from the low brilliance of standard IR radiation sources like globars, from the measurement technique (e. g., Fourier-transform [FT-IR]) itself, from the nonideal optical properties of polarizers and compensators, from the low detectivity of standard pyroelectric detectors, as well as from low optical throughput. Furthermore, the materials used for optical elements can impact sensitivity and restrict the accessible spectral range.

MM ellipsometers rely on generating and projecting a sufficient number of different polarization states in order to probe the sample's full MM. For polarization-space sampling, many ellipsometer designs employ dual-rotating compensators or a multiple-photoelastic-modulator configuration, while polarizers are typically fixed (non-rotating) to avoid problems with source polarization and detector polarization sensitivity. In such designs, the radiation must pass through all optical elements during the whole measurement process. Hence, all 16 MM entries are affected by a non-optimal throughput limited by the optical properties of these elements.

In a recent publication,[17] we presented a novel IR MM ellipsometer that is based on a different design and measurement approach. The ellipsometer measures the upper-left 3×3 MM block via different polarizer/analyzer settings, while both retarders are retracted from the optical path. These first 9 of the 16 MM elements are therefore least afflicted by noise. Optional retarders are only used to measure the fourth row or column of the MM. Tandem polarizers guarantee an optimized polarization control necessary to accurately determine

[a)] Electronic mail: andreas.furchner@isas.de

the block-offdiagonal MM elements. For temporal resolutions of a few minutes, the measurement scheme is centered around subsets of defined polarizer/retarder settings for generating and projecting pure polarization states, allowing one to extract quadruples of MM elements.

In this contribution, we have significantly optimized the instrument for full 4×4 Mueller-matrix measurements with increased signal-to-noise, high throughput, and close-to-ideal optical elements. A modular polarizer design provides access to the widest spectral range of 8000–800 cm^{-1} (1.25–12.5 µm) at sensitivities of up to 10^{-4} in the normalized MM elements. Tiniest vibrational features frequently observed in the fingerprint region below 2000 cm^{-1} can be resolved by using high-transmittance free-standing wire-grid polarizers, which provide an unprecedented sensitivity of up to $5\cdot10^{-5}$, even in the block-offdiagonal MM elements. Such advances in S/N ratio enable full 4×4 MM measurements and quantitative analyses of depolarizing and/or anisotropic thin films down to the nanometer level.

For many depolarizing thin-film samples, one often encounters a 2×2 block structure of the infrared Mueller matrix that looks similar to the characteristic structure of a non-depolarizing surface. The latter can be expressed by[5]

$$\mathrm{M}=\begin{bmatrix} \frac{1}{2}(|r_{pp}|^2+|r_{ss}|^2+|r_{ps}|^2+|r_{sp}|^2) & \frac{1}{2}(|r_{pp}|^2-|r_{ss}|^2+|r_{ps}|^2-|r_{sp}|^2) & \Re(r_{pp}r_{sp}^*+r_{ps}r_{ss}^*) & \Im(r_{pp}r_{sp}^*+r_{ps}r_{ss}^*) \\ \frac{1}{2}(|r_{pp}|^2-|r_{ss}|^2-|r_{ps}|^2+|r_{sp}|^2) & \frac{1}{2}(|r_{pp}|^2+|r_{ss}|^2-|r_{ps}|^2-|r_{sp}|^2) & \Re(r_{pp}r_{sp}^*-r_{ps}r_{ss}^*) & \Im(r_{pp}r_{sp}^*-r_{ps}r_{ss}^*) \\ \Re(r_{pp}r_{ps}^*+r_{sp}r_{ss}^*) & \Re(r_{pp}r_{ps}^*-r_{sp}r_{ss}^*) & \Re(r_{pp}r_{ss}^*+r_{sp}r_{ps}^*) & \Im(r_{pp}r_{ss}^*-r_{sp}r_{ps}^*) \\ -\Im(r_{pp}r_{ps}^*+r_{sp}r_{ss}^*) & -\Im(r_{pp}r_{ps}^*-r_{sp}r_{ss}^*) & -\Im(r_{pp}r_{ss}^*+r_{sp}r_{ps}^*) & \Re(r_{pp}r_{ss}^*-r_{sp}r_{ps}^*) \end{bmatrix}. \quad (2)$$

Our measurement approach ensures lowest noise in the upper-left 2×2 MM block, which contains key amplitude information. The other three 2×2 MM blocks comprise phase information related to co-polarization (*pp*, *ss*) and cross-polarization (*ps*, *sp*). Noise is also reduced for MM elements in the third row and column. Block-offdiagonal elements usually show much weaker IR signatures. In such cases, our data-acquisition scheme enables one to specifically increase S/N for particular MM elements. Further S/N enhancement is possible when the complete 4×4 MM is measured, in which case matrix filtering methods can be applied.[5]

Acquiring high-quality MM data is often merely the first step in sample characterization and quantification. The ever-growing complexity of layer stacks, structured surfaces, and depolarizing thin films also demands the advancement of theoretical models to interpret the data.

In this contribution, we apply the IR MM ellipsometer with its unique capabilities, such as the broad spectral range and unsurpassed S/N, to obtain comprehensive 4×4 MM data of three sample systems. Each system poses a different challenge regarding quantitative analysis. We describe diverse optical modeling approaches to quantify the data and to extract information concerning the optical and physical sample properties.

The first set of samples are uniaxially anisotropic and depolarizing polyimide-based microporous membrane thin films for gas separation purposes. These membranes are strongly heterogeneous, which impacts the measured polarization degree over a wide spectral range, thus requiring broadband experimental data to accurately determine their optical properties.

The second example is a 32 nm thin polyimide film (PI2611) with applications in gas sensors and electronic devices. Upon surface rubbing, the molecules inside the polymer layer can be realigned. We make use of the ellipsometer's excellent S/N to quantify the corresponding changes in optical film properties from uniaxial to biaxial anisotropy.

Lastly, we investigate two-dimensional silica arrays suitable for use in sensor applications. These trapezoid-shaped structures have profile dimensions in the µm range that give rise to complicated MM spectra. Here the wide accessible spectral range of the ellipsometer proves crucial for probing the relevant structure parameters. We employ rigorous coupled-wave analysis (RCWA) to model and quantify array profile and orientation, highlighting the possibilities of broadband IR MM ellipsometry for applications such as process control and quality management.

II. EXPERIMENTAL SECTION

A. Ellipsometer Configuration

The infrared Mueller-matrix ellipsometer (Fig. 1) operates both in reflection geometry, with possible incidence angles between $\varphi_0 = 45^\circ$ and 90°, and in transmission. Naturally, reflection mode provides the highest sensitivity for characterizing nanometer-thin films. A tilt- and height-adjustable rotation stage with autocollimation unit is used for sample alignment and azimuthal orientation. The ellipsometer's input arm is fixed, whereas sample stage and analyzer arm are mounted on a motorized, independently angle-adjustable 2ϑ goniometer stage (2-Circle Goniometer 423, Huber Diffraction and Positioning Equipment, Germany). An FT-IR spectrometer (Tensor 37, Bruker, Germany) with a globar as radiation source is coupled to the ellipsometer.

Input and output arm of the instrument contain the optical elements of the polarization-state generator (PSG) and analyzer (PSA), respectively. PSG and PSA are modularly designed and each consist of a tandem pair of aligned polarizers as well as optional, non-rotating retarders mounted on motorized translation stages for reproducible retarder insertion into, or retraction from, the optical path.

Using tandem polarizers suppresses unwanted leaking polarization states, thereby improving the ellipsometer's polariza-

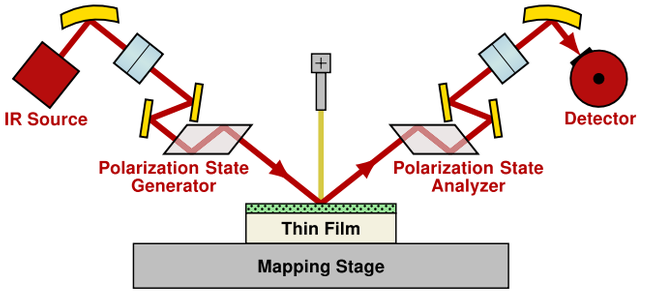

FIG. 1. Schematic of the infrared 4×4 Mueller-matrix ellipsometer.

tion control. Holographic KRS-5 wire-grid polarizers (25 mm clear aperture, 0.25 µm wire spacing, Specac Ltd, England) provide access to the broadest spectral range of 8000–800 cm^{-1}. Free-standing Au wire-grid polarizers (P03, InfraSpecs, Germany, 5000–800 cm^{-1}) can be engaged when enhanced S/N is required below 2000 cm^{-1}.

The retarder units consist of a rhombic KBr prism for two phase-shifting attenuated total reflections, and two gold mirrors for beam repositioning.[18] A phase shift between *p*- and *s*-polarization close to 90° yields an almost achromatic retarder response. The utilized polarizers and retarders enable the generation and projection of close-to-ideal purely linear and circular polarization states.

Off-axis parabolic mirrors focus the IR radiation onto sample and detector. The latter is mounted on a translation stage for optimal focusing. A photovoltaic mercury-cadmium-telluride detector (MCT, KLD-1-J1-3/11, Kolmar Technologies, USA) is used to avoid non-linearity issues, while providing orders of magnitude higher detectivity compared to standard pyroelectric detectors.

The whole instrument is constantly purged with dried air (r. H. $\ll 0.1\%$) to ensure atmospheric stability and minimal IR absorption from CO_2 and H_2O vapor.

B. Measurement Principle

According to the MM calculus,[19] the output Stokes vector S_{out} at the detector, which characterizes the light's polarization state after interaction with sample and ellipsometer optics, is derived from

$$\begin{aligned} S_{out} &= PSA^T \cdot M \cdot PSG \\ &= D \cdot A \cdot R_2 \cdot \begin{bmatrix} M_{11} & M_{12} & M_{13} & M_{14} \\ M_{21} & M_{22} & M_{23} & M_{24} \\ M_{31} & M_{32} & M_{33} & M_{34} \\ M_{41} & M_{42} & M_{43} & M_{44} \end{bmatrix} \cdot R_1 \cdot P \cdot S_{in} \end{aligned} \quad (3)$$

where M is the Mueller matrix of the sample; P and A are the polarizer and analyzer matrices; R_m the retarder matrices; $S_{in} = [s_0, s_1, s_2, s_3]^T$ is the input Stokes vector in front of the first polarizer, with $s_i/s_0 \neq 0$ implying source prepolarization; and D is the detector Mueller matrix.

In general, a minimum number of $4 \times 4 = 16$ sufficiently different polarization states must be generated in the PSG and projected in the PSA in order to measure a full 4×4 Mueller matrix. An optimum choice results for such combinations of

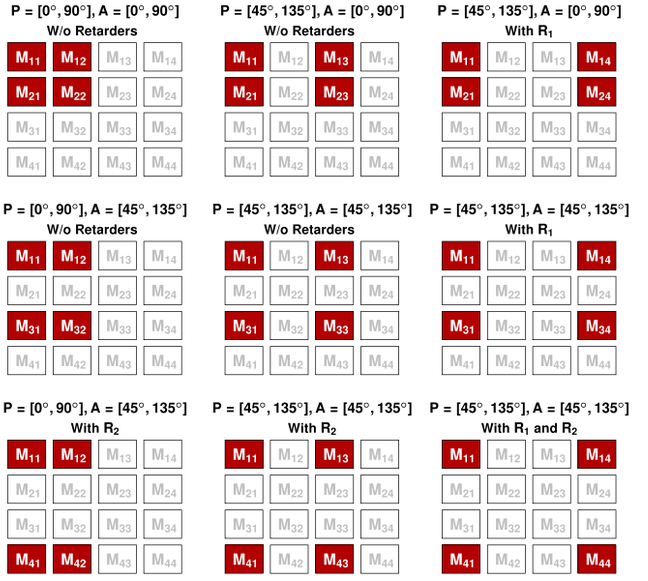

FIG. 2. Quadruples of MM elements measured from different combinations of polarizer/analyzer/retarder settings. Figure from Ref.[17]. ©2018 Optical Society of America.

(usually mixed) polarization states that inscribe regular tetrahedra on the Poincaré sphere.[20] For the sake of thin-film sensitivity and noise reduction, however, we chose to work with the six pure polarization states $[1,\pm1,0,0]^T$, $[1,0,\pm1,0]^T$, and $[1,0,0,\pm1]^T$, i. e., with octahedral sampling.[21] These states can be obtained by ideal PSGs and PSAs. Four intensity measurements with such PSG/PSA vectors in Eq. (3) lead to a set of four equations solvable for a subset of four MM elements at a time.[19] By using different PSG/PSA combinations, the whole 4×4 MM can be deduced.

We have adapted this approach for the presented ellipsometer and derived generalized equations that account for source polarization, polarizer diattenuation, and other nonidealities.[17]

In practice, the pure polarization states are realized according to Fig. 2 by appropriate rotation of the polarizers to 0°/90° (linear polarization), to 45°/135° (linear diagonal polarization), or by combining the latter settings with a 90° phase-shifting retarder (circular polarization). In other words, for maximum optical throughput, and hence improved S/N, the upper-left 3×3 MM block is acquired without retarders in the optical train. The first three MM elements in the 4th column and row are obtained with 1st or 2nd retarder present, respectively. Only M_{44} requires the use of both retarders.

C. Data Processing

Having the sample's full 4×4 Mueller matrix at hand allows for the application of matrix filtering methods. Measured MMs were subjected to covariance filtering, which can further reduce polarimetric noise.[5,22,23] Principal-component covariance filtering, which retains only the non-depolarizing information of the MM, was applied to MM data of the non-depolarizing, 32 nm thin PI2611 film. Routines for covariance filtering were

adapted from Matlab code provided by Razvigor Ossikovski (LPICM, Ecole Polytechnique, France).

Data evaluation was performed by Levenberg–Marquardt fitting minimizing the reduced χ^2, i. e., the sum of all error-weighted squared differences between measured and calculated MM elements.[1] All presented MM data are normalized to their respective M_{11} elements.

III. RESULTS

A. Depolarizing, Heterogeneous Polymer Films with Uniaxial Anisotropy

Polymers of intrinsic microporosity[24] (PIMs) are a recently discovered group of organic polymers featuring extremely rigid, contorted backbones that prevent efficient molecular packing. This packing inefficiency results in the formation of micropores in the size scale of small molecules (< 2 nm), rendering PIMs highly attractive for gas separation applications.

Ogieglo et al.[25] used polyimide (PI) based PIMs as a precursor to fabricate gas-separating carbon molecular sieve membranes. Different membranes were created by altering the precursor film's structural properties via pyrolysis at temperatures ranging from 500°C to 1000°C. Polyimide pyrolysis induces chemical and structural changes leading to a unidirectional layer collapse enforced by the presence of the substrate. This collapse manifests in the film's optical properties, namely, in marked optical anisotropy. Ellipsometry in the ultraviolet–visible–near-IR spectral range was successfully used to quantify the degree of anisotropy[25] as the films progressed from being almost isotropic at low pyrolysis temperatures to being highly uniaxially anisotropic at elevated temperatures.

Here we employ IR MM ellipsometry to follow the optical, chemical, and structural changes as evidenced by changes in film thickness and uniaxial dielectric function. We focus on two films prepared on silicon substrates: a pristine one (415 nm thick) exposed to 50°C, and a collapsed one (263 nm thick) that underwent pyrolysis at 600°C.

Figure 3 shows the PIM-PI molecular structure along with typical optical images in size relation to the measurement area of the IR spot, as well as experimental and fitted MM data of the pristine film at multiple incidence angles between $\varphi_0 = 45°$ and 80°. The challenge in extracting the films' optical properties from the measured MM spectra is that the PIM-PI layers exhibit pronounced thickness inhomogeneities, seen already in the optical images. Thickness variations of up to ±150 nm within the measured spot lead to substantial drops in polarization degree to values as low as 11%. Standard optical models for non-depolarizing samples thus fail to work.

In order to properly quantify the complex dielectric function, particularly the anisotropic vibrational signatures between 2000–800 cm^{-1}, optical modeling of the data has to account for the thickness non-uniformity. In essence, MM elements are calculated by averaging over the measured area assuming that multiple different film thicknesses contribute to the observed signals. As a consequence, the polarization degree diminishes and follows a characteristic spectral behavior depending on incidence angle and thickness distribution. The resulting agreement between measured and fitted MM data in Fig. 3 shows that such modeling of inhomogeneous films is in fact feasible. We now explain the modeling process in more detail.

Since the MM is blockdiagonal, as is expected for a uniaxially anisotropic (or isotropic) film,[5,26] it is convenient for further discussions to switch to the more familiar Ψ/Δ representation of the data, given by

$$\mathrm{M} = \frac{|r_p|^2+|r_s|^2}{2}\begin{bmatrix} 1 & -\cos 2\Psi & 0 & 0 \\ -\cos 2\Psi & 1 & 0 & 0 \\ 0 & 0 & \sin 2\Psi\cos\Delta & \sin 2\Psi\,\sin\Delta \\ 0 & 0 & -\sin 2\Psi\,\sin\Delta & \sin 2\Psi\cos\Delta \end{bmatrix}. \quad (4)$$

Measured spectra were fitted with a stratified layer model (Air–PIM-PI–SiO_2–Si). The anisotropic dielectric function of the uniaxial PIM-PI layer was described as a sum of Lorentzian oscillators[4] associated with PIM-PI's molecular vibrational modes. To reduce the number of fit parameters and avoid parameter correlations, oscillator frequencies and line widths for in-plane (xy) and out-of-plane (z) directions were assumed to be identical, but oscillator strengths were allowed to differ.

In a first approach, we restricted the fit's spectral range to below 2000 cm^{-1}, where depolarization is seemingly negligible (Pol. Degree > 0.98). The PIM-PI layer was assumed to be uniform and fitted with a single, average thickness.

In a second, more sophisticated approach, the complete spectral range up to 8000 cm^{-1} was fitted, and film thickness was modeled as non-uniform, following a certain thickness distribution, as proposed by Jellison et al.[27] In other words, depolarization was taken into account. Beside film heterogeneity, depolarization can also arise from the ellipsometer's instrument function, which is dominated by effects of the device's opening angle (about ±2°). Averaged MM elements were therefore

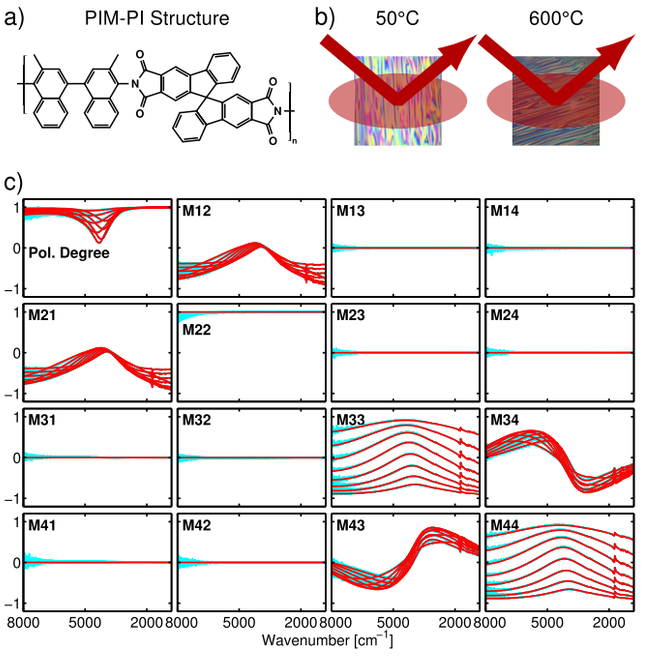

FIG. 3. a) PIM-PI molecular structure. b) Optical images (50°C and 600°C film) in relation to the spot size of the IR MM ellipsometer. c) Experimental (turquoise) and fitted (red) MM data of the pristine film (50°C) at incidence angles between 45° and 80° in steps of 5°.

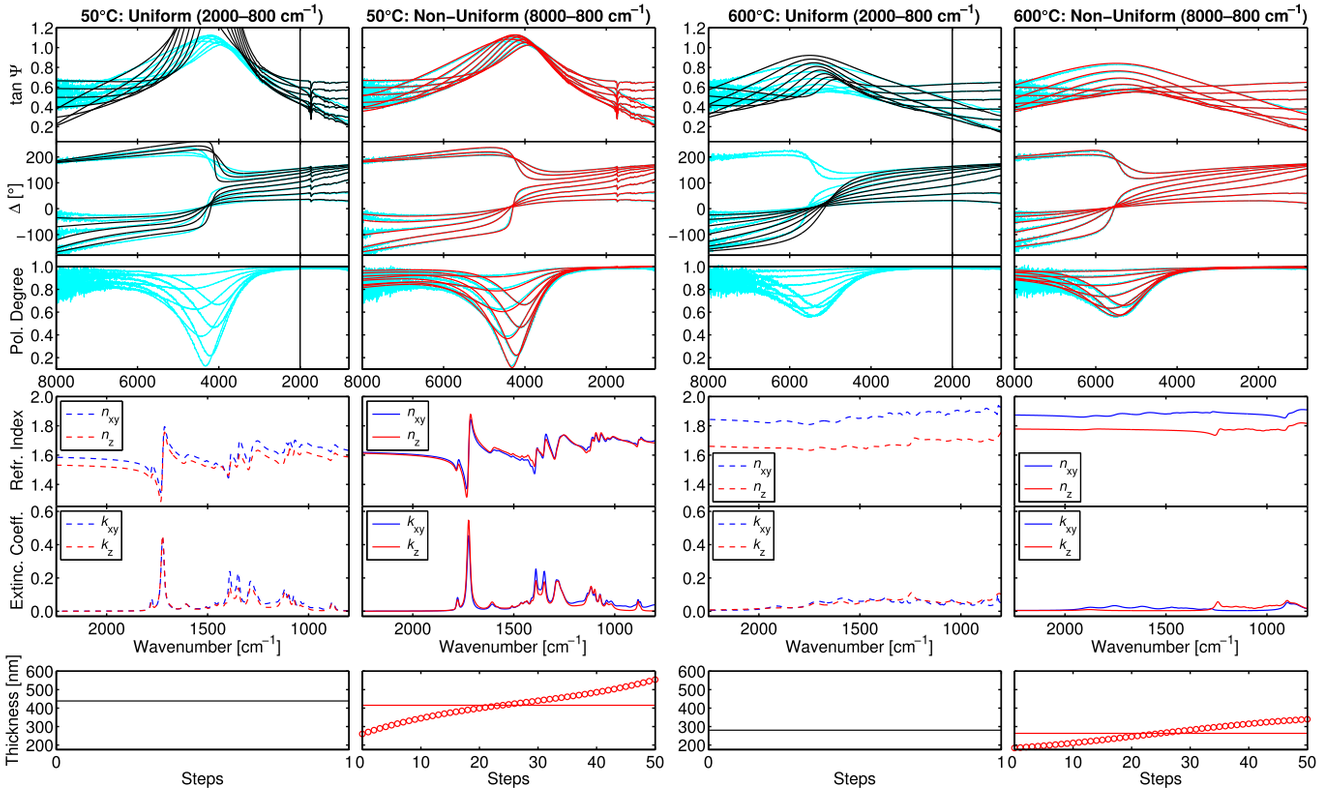

FIG. 4. Measured (turquoise) and fitted (black, red) PIM-PI spectra at incidence angles between 45° and 80° in steps of 5°. $\tan\Psi$ and Δ are the effective ellipsometric parameters corresponding to the averaged MM elements in Eq.(5). The left two columns are data of the pristine (50°C), almost isotropic film. The right two columns are data of the pyrolyzed (600°C), highly uniaxially anisotropic film. Refractive indices and extinction coefficients were extracted from the fits assuming the film thickness is either uniform (fit restricted to below 2000 cm^{-1}) or non-uniform, with fitted thickness distributions shown below.

computed according to

$$\overline{\mathrm{M}}_{ij} = \iint D(d)\,\Phi(\varphi_0)\,\mathrm{M}_{ij}\,\mathrm{d}d\,\mathrm{d}\varphi_0 \tag{5}$$

by integrating over both the thickness distribution $D(d)$ and the incidence-angle distribution $\Phi(\varphi_0)$.

The polarization degree P we define by

$$P = \sqrt{\overline{\mathrm{M}}_{12}^2 + \overline{\mathrm{M}}_{33}^2 + \overline{\mathrm{M}}_{43}^2} \leq 1 \tag{6}$$

then shows a characteristic spectral dependence on thickness and angle of incidence.

In a first pass, $D(d)$ was taken to be a linear function to approximate the observed $P(\varphi_0)$ dependence. Subsequently, $D(d)$ was refined as a 3rd-degree polynomial. 50 thickness steps turned out to be sufficient to describe the measured data.

Measured and fitted data as well as results of thicknesses and optical constants (n and k) obtained from the two modeling approaches are contrasted in Fig. 4. With 439 nm vs. 415 nm and 280 nm vs. 263 nm, the uniform and non-uniform film method yield similar average film thicknesses for the pristine and the 600°C film, respectively. Only the non-uniform film model can describe the dampening effects from the drop in polarization degree that significantly influence $\tan\Psi$ and Δ above 3000 cm^{-1}. Yet, for both approaches, measured and fitted data of the two PIM-PI films agree within the small spectral window between 2000–800 cm^{-1}. However, the corresponding optical constants differ quite substantially. Especially for the 600°C sample, which exhibits strong out-of-plane anisotropy, n and k values are unreliable if the film heterogeneities are not accounted for.

Comparing the optical constants obtained from the uniform and non-uniform approach demonstrates that even small deviations of the polarization degree from unity can easily be mistaken for pronounced anisotropy if only a narrow spectral range is considered and depolarization is disregarded. Looking at a wider spectral range can reveal the true nature of the film's structural properties and is often necessary for the correct determination of its optical properties. This point is best illustrated for the in-plane and out-of-plane refractive indices of the pristine (50°C) PIM-PI film. As seen in Fig. 4, the uniform model yields substantial baseline differences between n_{xy} and n_z, i. e., birefringence related to the respective high-frequency dielectric constants. These differences diminish markedly if the non-uniform model is applied. For instance, birefringence at, and above, 2250 cm^{-1} reduces by a factor of 10 from about $n_{xy} - n_z = 0.054$ for the uniform to $n_{xy} - n_z = 0.006$ for the non-uniform model, meaning the contributions to the suscepti-

bility due to higher-energetic electronic transitions are almost isotropic, in accordance with Ref.[25].

The IR optical constants reveal dramatic changes in the polymer's vibrational fingerprint reflective of the pyrolysis-induced chemical transformations. Various chemical reactions, such as the removal of CO, CO_2, H_2, or N_2,[28] lead to a structural collapse accompanied by carbon enrichment and an increasing degree of conjugation, i. e., partial graphitization. Compared to the 50°C pristine sample, these chemical pyrolysis effects in the 600°C film significantly diminish the imide-associated carbonyl-stretching bands between 1800–1675 cm^{-1}, as well as virtually all other bands at lower wavenumbers associated with the previously chemically intact PI molecular structure. The film's overall dielectric function becomes rather featureless, which is typical for a turbostratic, highly conjugated carbon matrix.[29] The remaining broad spectral signatures are mainly associated with vibrational modes of fused aromatic rings that occur in the microporous structure of such carbon molecular sieves after pyrolysis at 600°C.[30]

We stress that the simultaneous fits on thickness distribution and dielectric function were only possible because the ellipsometer provided access to a broad spectral range. In conjunction with a sufficient number of measurements at different incidence angles, the wide spectral range allowed the accurate modeling of the polarization degree, and hence the decorrelation of film thickness distribution and anisotropic optical constants.

B. Non-Depolarizing, Homogeneous Polymer Thin Films with Biaxial Anisotropy

In this example, we investigate an ultrathin polyimide film (PI2611, DuPont) on silicon for its anisotropic Mueller-matrix vibrational fingerprint. After precursor spincoating and thermal annealing,[31] PI2611 layers typically exhibit uniaxial optical anisotropy. Films of 1.81 µm and 84 nm thickness have previously been thoroughly investigated using generalized IR ellipsometry,[31,32] and average molecular orientations could be deduced.

Polyimide layers find wide applications in microelectromechanical systems (MEMS), sensors, and liquid-crystal devices.[33–37] For the latter, correct in-plane orientation of the rod-like molecular units is often required. The alignment of PI molecules can be influenced, for instance, via defined surface rubbing.[33,35,38]

Here we utilize IR MM ellipsometry to quantify such alignment effects. The aim is to test the thin-film limits of block-offdiagonal MM analysis by probing small changes from uniaxial to biaxial anisotropy in a 32 nm thin, molecularly reoriented PI layer. For this purpose, we used a polyester microfiber cloth to partially align the molecules inside the originally uniaxial polyimide film. The surface was manually rubbed several times along an axis about 5° to 10° off the sample's nominal x-axis.

Figure 5 shows that rubbing has an obvious effect on the block-offdiagonal MM elements measured at different azimuthal sample orientations. For the uniaxial film before molecular realignment, the block-offdiagonal MM elements are zero, whereas they become nonzero in the aligned, biaxial case, if

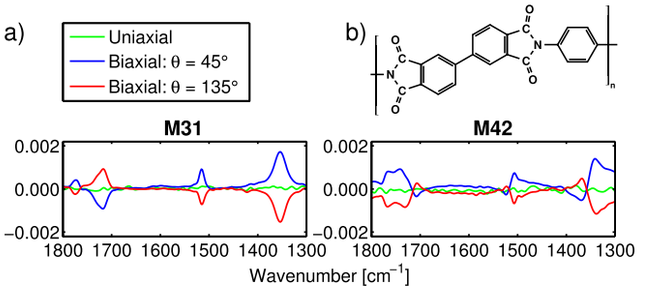

FIG. 5. a) Selected MM elements at $\varphi_0 = 45°$ and different azimuthal rotations of the 32 nm PI2611 film in its uniaxial state before rubbing and its biaxial state after rubbing. b) Molecular structure of PI2611.

measured off an optical axis. This observation is in line with Eq. (2), from which one expects a block-diagonal form of the uniaxial film's MM with zero-valued block-offdiagonals ($M_{13} = M_{31} = M_{23} = M_{32} = M_{14} = M_{41} = M_{24} = M_{42}$), and a fully populated form in the biaxial case.[5,26]

The ellipsometer is sensitive enough to resolve even tiny vibrational signatures with MM amplitudes below $5 \cdot 10^{-4}$. Prominent vibrational features, related to the PI molecular structure given in Figure 5, are the ν(C−N−C) stretching band around 1355 cm^{-1}, the ν(C=C) band of the PDA (phenylenediamine) ring, and the stretching modes of the imide ring's two C=O groups. These carbonyl vibrations are visible as in-phase and out-of-phase ν(C=O) modes at 1775 cm^{-1} and 1715 cm^{-1}, respectively, with a smaller contribution at 1725 cm^{-1} that is likely to arise from packing perturbations of the imide ring structures.[39]

Similar to the microporous polymer membranes discussed before, we used an anisotropic oscillator layer model to quantify the PI film's MM optical response. Multiple incidence and azimuth angles were fitted with a single thickness and with unconstrained oscillator parameters in x-, y- and z-directions. The fit revealed an azimuthal orientation of $8° \pm 2°$ of the film's in-plane optical axes with respect to the ellipsometer coordinate system, which corresponds well to the nominal rubbing direction.

Exemplary experimental and fitted 4×4 MM data at four azimuths are shown in Fig. 6. The measured complex lineshapes, particularly observed in the block-offdiagonal MM elements, are reproduced by the biaxial optical model. In-plane anisotropy resulting from the rubbing procedure appears to be small, though, as the block-offdiagonal MM elements contain only relatively minute vibrational features.

The change in optical anisotropy is more obvious when comparing the uniaxial and biaxial optical constants obtained from the respective fits before and after rubbing. Such a comparison is presented in Fig. 7. Indeed, the in-plane optical properties (x vs. y) of the biaxial film differ only by a few percent, indicating that the polyimide molecules were only slightly realigned.

A closer inspection of the optical constants reveals subtle changes in PI2611's vibrational bands, for example, in the out-of-phase carbonyl stretching modes. Upon rubbing, a peak arises in k_x and k_y at 1732 cm^{-1} in the biaxial state that was only visible as a small shoulder in the uniaxial state. This band

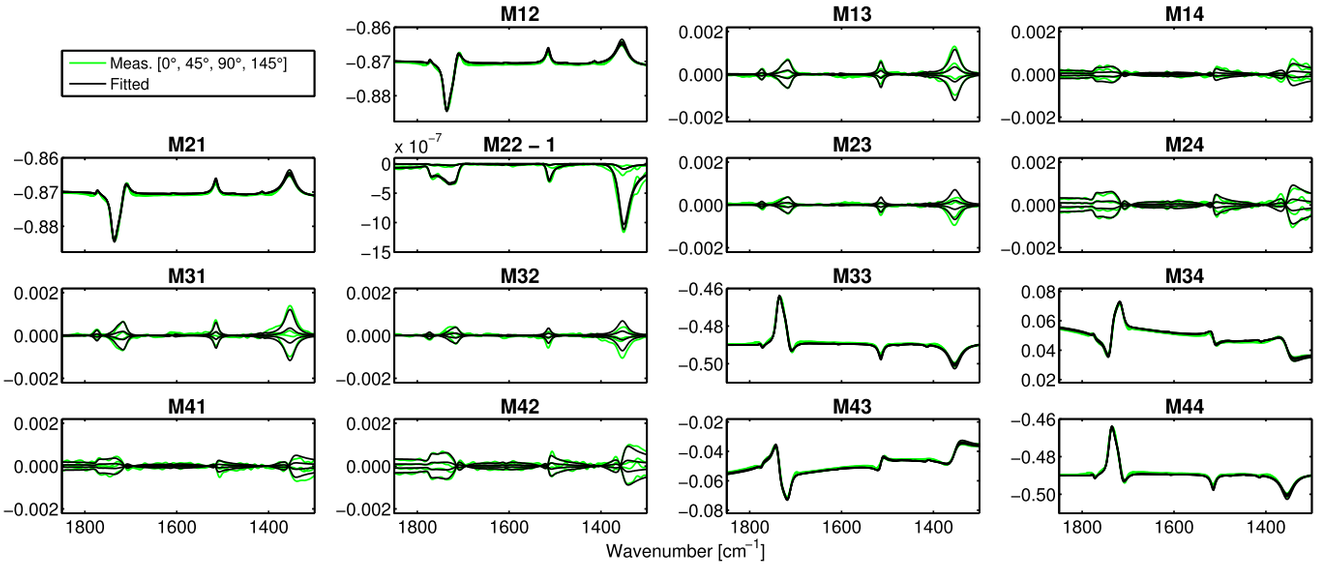

FIG. 6. Measured and fitted MM data of the rubbed, biaxially anisotropic, 32 nm thick PI2611 film at $\varphi_0 = 65°$ and four azimuthal rotations.

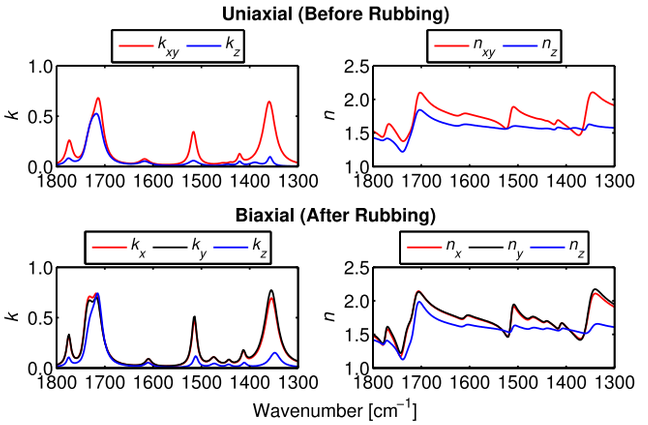

FIG. 7. Anisotropic optical constants of the PI2611 film in its uniaxial state before and its biaxial state after molecular realignment.

component can be assigned to imide-ring distortions or perturbations of molecular packing, i. e., steric disturbations, which also causes a shift in the ν(C=O) oscillator force constant, and hence frequency, compared to the unperturbed component at 1715 cm^{-1}.[39]

The observed changes in band composition suggest that rubbing not only leads to an overall small realignment of the polyimide molecules, but that it also slightly disturbs the molecular packing. Our findings are in agreement with Hietpas et al.[39] who reported similar ν(C=O) band compositions and lineshapes for aligned, stacked layers of BPDA–PDA polyimides.

More detailed investigations of rubbing effects on molecular orientations and band compositions are the objective of upcoming studies. These first quantitative results, however, already demonstrate the use of IR 4×4 MM ellipsometry for sensitively probing small changes of biaxial anisotropy in nanometer thin organic films. Future work will aim at in-depth characterization of anisotropic and/or depolarizing polymer and protein thin films, also in combination with liquid flow-cells for *in situ* IR MM studies of such sample systems.

C. 2D-Structured Trapezoidal Silica Arrays

In the third example, we use the MM ellipsometer for detailed measurements of µm-sized SiO_2 arrays with rectangular base and trapezoidal profile. A schematic and an SEM (scanning electron microscopy) topview of such arrays are depicted in Fig. 8. The structures were prepared from an H = 1000 nm thick SiO_2 layer on a Si wafer by photolithographic processing with subsequent wet-chemical etching.[17] Their characteristic structure parameters are the trapezoid's period lengths (P_x, P_y), base widths (B_x, B_y), and top widths (T_x, T_y).

As seen in the SEM image, the structures are not perfect. They exhibit some defects, such as holes and crooked edges, at every other trapezoid. Corners and slopes are also slightly rounded. These deviations from an ideal array are expected to influence the sample's experimental Mueller matrix. As a result of the array's geometrical complexity, with all profile parameters being in the µm range, the infrared MM is correspondingly rich in spectral features.

For a quantitative evaluation it is important that such a structured surface no longer constitutes a homogenizable medium. Therefore, we aim to understand the measured IR spectra by combining MM ellipsometry with RCWA-based optical modeling. This approach allows us to quantify the array's profile and orientation, as well as to assess its fabrication quality. The latter is related to symmetries and polarization index[40]

$$\mathrm{PI} = \sqrt{\left(\sum \mathrm{M}_{ij}^2/\mathrm{M}_{11}^2 - 1\right)/3} \qquad (7)$$

of the measured Mueller matrix.

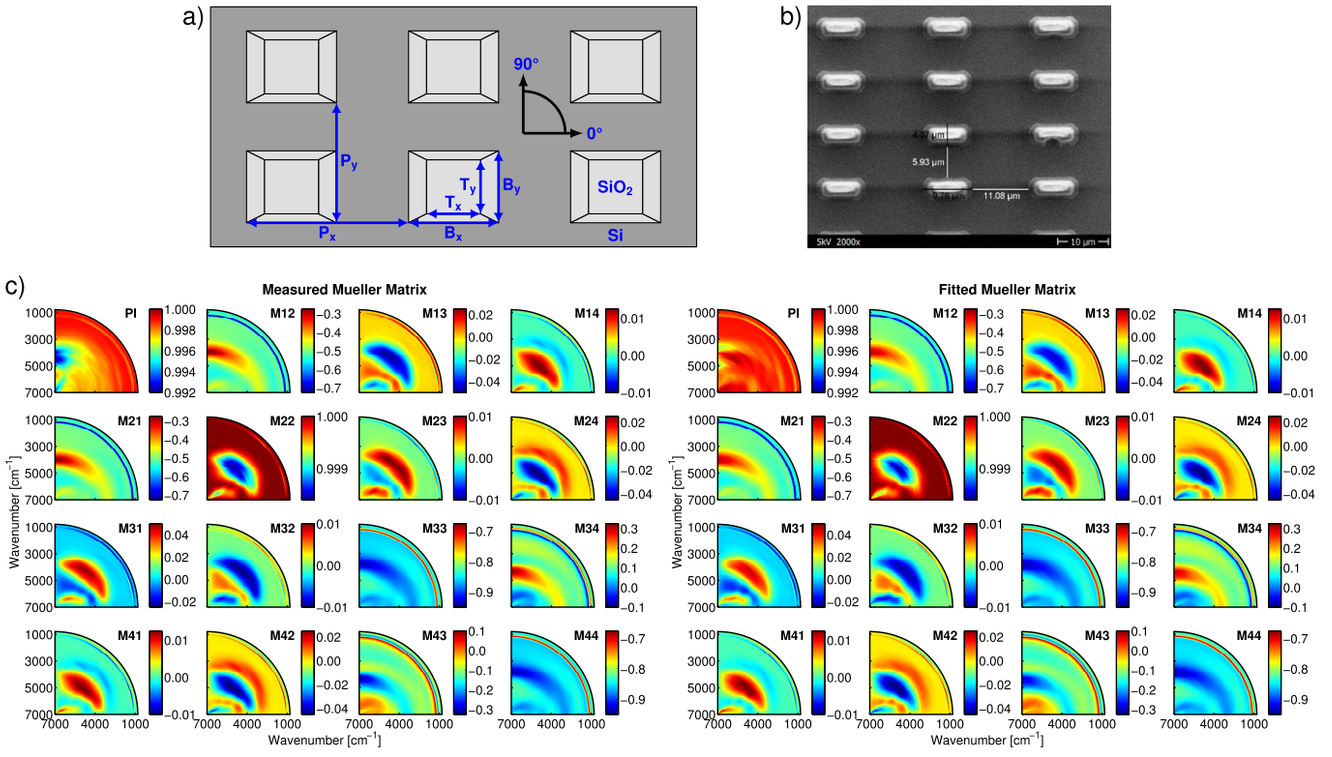

FIG. 8. a) Schematic topview of the trapezoidal SiO_2 arrays on Si with marked structure parameters. b) SEM image of the investigated surface. c) Radial plots of measured (left) and fitted (right) MM elements and polarization index at azimuths between 0° (horizontal) and 90° (vertical).

Figure 8 shows measured and fitted broadband (7000–800 cm^{-1}) MM data at 50° incidence angle and azimuthal sample rotations between 0° and 90°. The data is presented in polar form, with radial distance and angular position corresponding to spectral position and azimuthal sample rotation, respectively.

The MM is dominated by the vibrational signatures of the trapezoid material's SiO_2-stretching modes, $\nu(SiO_2)$, around 1100 cm^{-1}, as well as by structure-related broad spectral patterns that are particularly intense on the MM's 2×2 blockdiagonal. These spectral features are modulated upon sample rotation by the varying space between the periodically aligned trapezoidal structure elements.

The blockdiagonal MM elements (M_{12}, M_{21}, M_{22}; M_{33}, M_{34}, M_{43}, M_{44}) are nonzero at all azimuths. In contrast, the block-offdiagonal MM elements vanish along symmetry axes. This pseudo-isotropic case approximately occurs at the nominal azimuths of 0° and 90°, where the plane of incidence coincides with the sample's x- and y-axis, respectively. For all other sample rotations, the MM is fully populated and shows anisotropy effects in all matrix elements, such as distinctly different, azimuth-dependent lineshapes of the $\nu(SiO_2)$ band in the various MM elements. It is the nonzero block-offdiagonal MM elements that render the MM highly sensitive towards the array's orientation and structure parameters, enabling sufficient parameter decorrelation in a fit.

Data fitting was performed in SpectraRay 3 (Sentech Instruments GmbH) based on RCWA calculations.[41,42] The SiO_2 trapezoid structures were sliced into three vertical sublayers to approximate their slopes. Nine diffraction orders were taken into account to accurately model the short-wavelength spectral range. A numerical aperture of NA = 0.04 was simulated to reproduce the impact of the ellipsometer's opening angle on the observed polarization index, which would otherwise be 1 for an ideal array.

Figure 8 shows that measurement and fit are in remarkable agreement. The fitted MM data follow not only the broad spectral features but also the smaller effects that arise in the block-offdiagonal elements from the array's unequal profile parameters in x- and y-direction. Moreover, the different $\nu(SiO_2)$ lineshapes are correctly described.

The fit reveals a sample orientation of 0.5° off its nominal axis. Results for array height and structure parameters are listed in Table I and compared to nominal values obtained from SEM image analysis. Also stated are the volumes of a single trapezoid and the unit cell of the periodic structures. From these, SiO_2 surface coverages of less than 10% are deduced. IR MM ellipsometry combined with RCWA can resolve profile information at such low coverage because it is the array structures themselves that generate non-negligible entries in the block-offdiagonal MM elements. Both SEM and RCWA deliver similar results for all profile parameters. This demonstrates that IR MM ellipsometry bears great potential as a nondestructive method for structure quantification, rendering the technique highly relevant for process control and in-line monitoring.

TABLE I. Nominal and fitted array profile parameters, volumes of single trapezoid and unit cell, as well as SiO_2 surface coverage.

Parameter	Nominal (SEM)	Fitted (RCWA)
H [µm]	1.00 ± 0.05	1.00 ± 0.02
P_x [µm]	20.8 ± 0.2	20.2 ± 0.5
P_y [µm]	10.3 ± 0.3	9.9 ± 0.6
B_x [µm]	9.8 ± 0.2	10.6 ± 0.6
B_y [µm]	4.4 ± 0.5	5.3 ± 0.4
T_x [µm]	4.7 ± 0.8	5.1 ± 0.4
T_y [µm]	1.4 ± 0.9	2.2 ± 0.4
V_{trap} [µm^3]	22 ± 8	30 ± 5
V_{unit} [µm^3]	449 ± 52	468 ± 57
Coverage [%]	4.9 ± 2.0	6.6 ± 1.9

Polarization index and symmetries of the Mueller matrix are important measures regarding the array's fabrication quality. Certain symmetries are expected as a consequence of the electromagnetic reciprocity theorem for Mueller matrices of symmetric structures.[40,43] In particular, $M_{12} = M_{21}$, $M_{13} = -M_{31}$, $M_{23} = -M_{32}$, $M_{14} = M_{41}$, $M_{24} = M_{42}$, and $M_{34} = -M_{43}$. These symmetries are indeed observed in the measured Mueller matrix. However, small asymmetries are found between the lower-left and upper-right 2×2 MM blocks, especially at larger azimuths. These differences also impact the MM's polarization index.

To a large extent, the measured deviations of the polarization index from unity are a result of the ellipsometer's opening angle, and are thus partially described by the RCWA model. Measured and fitted polarization index agree in the material-specific $\nu(SiO_2)$ signatures around 1100 cm^{-1}, and in the geometry-related features around 5000 cm^{-1}, 3500 cm^{-1}, and 2100 cm^{-1}. It turns out that the array's particular combination of profile parameters renders the 4800–3800 cm^{-1} range most sensitive towards structure variations. The largest deviation between the polarization indices is thus found in this region. The differences are indicative of a slight lack of structural symmetry. We therefore attribute them to the above-mentioned defects visible with SEM. However, the absolute differences are small, corresponding to less than 0.5% depolarization, and hence suggest macroscopic homogeneity of the array structure.

Future studies will investigate in more detail the relationship between polarization index and array nonidealities. Thus far the polarization index proves to be a valuable quantity for improving the fit, and to be a potential marker for assessing the quality of the array.

Lastly, we point out that SEM image analysis covers only a limited number of structure elements, whereas IR MM ellipsometry can probe much larger footprints, up to the complete array. Regarding sensor, coating and photonics applications, ellipsometry can thus provide more reliable information on the performance of the array as a whole. Furthermore, SEM requires destructive cutting for sideview imaging and quantification of the array's base and top widths. In contrast, the combined approach of IR MM ellipsometry and RCWA delivers quantitative information in a nondestructive fashion. Knowledge of the profile parameters is crucial for further array processing, for anisotropy analysis of the used etching process, and for judging the optical performance of the 2D structure. Broadband infrared MM ellipsometry therefore proves promising as a versatile, nondestructive characterization tool.

IV. SUMMARY AND OUTLOOK

IR Mueller-matrix ellipsometry provides detailed information on chemical composition, molecular interactions, and structural properties of organic thin film and patterned surfaces by probing the material-specific vibrational bands and structure-related baselines found in the infrared. In this article, we have demonstrated in-depth sample analyses by combining IR MM ellipsometry with advanced optical simulations. For this purpose, we have developed a high-throughput-optimized broadband ellipsometer that achieves unprecedented MM sensitivity of up to $5 \cdot 10^{-5}$. The instrument enables a tailored approach for optimizing measurement time and signal-to-noise by selectively focusing on quadruples of MM elements, thus resolving even weak IR signatures often observed in block-offdiagonal elements. We have presented different optical modeling approaches for quantitative MM data evaluation based upon anisotropic layer stacks and rigorous coupled-wave analysis.

We used the MM ellipsometer to investigate profile and orientation of 2D arrays of trapezoidal silica microstructures. This example illustrates the usefulness of IR MM ellipsometry for process control, optimization, and quality monitoring. RCWA-based theoretical calculations enabled us to verify the SiO_2 chemical MM signatures and to quantify key structural parameters like profile height, periods and widths. Analysis of the polarization index obtained from the MM data suggested macroscopic homogeneity of the structure. For future applications, the use of low-energy IR radiation combined with IR fingerprint analysis could allow nondestructive investigations and quality control of photosensitive polymer masks prior to further processing. IR MM ellipsometry thus holds great potential for identifying both chemical and structural problems like distortion effects during manufacturing and processing.

Various complex polymer thin films were investigated. Polyimide membranes used for gas separation exhibited substantial thickness heterogeneity and pronounced depolarization. The broad accessible spectral range of 8000–800 cm^{-1} was fundamental to decorrelating and quantifying film thickness profile and uniaxial optical constants in a depolarization optical model. Furthermore, the ellipsometer's high S/N enabled a sensitive block-offdiagonal MM analysis of a 32 nm thin polymer film with biaxial anisotropy, demonstrating thin-film sensitivity even for complex anisotropic samples. These examples show the potential of IR MM ellipsometry for investigations of polymer, protein and related thin films. Future projects aim at *in situ* IR MM ellipsometry studies of solid–liquid interfaces.

Overall, IR MM ellipsometry provides new analysis possibilities in the fields of polymer, catalytic and biomedical materials, as well as optoelectronic and sensing devices. Comprehensive characterization of thin films and complex surface structures are becoming feasible by tapping the vast, but so far almost unused, potential of this technique.

ACKNOWLEDGMENTS

The authors are indebted to Matthias Zellmeier (HZB Berlin) for preparation of the trapezoidal SiO_2 arrays, to Timur Shaykhutdinov for expertise in RCWA simulations, to Uwe Richter (Sentech Instruments GmbH) as well as Ilona Engler, Cordula Walder and Özgür Savaş for technical assistance, to Margarita Günther (TU Dresden), Karin Sahre and Klaus-Jochen Eichhorn (IPF Dresden) for providing the PI2611 samples, and to Sentech Instruments GmbH for construction of the retarder units. Financial support through European Union grants (EFRE 1.8/13, ProFIT 10160255, 10160265, 10160256) as well as by the Ministerium für Innovation, Wissenschaft und Forschung des Landes Nordrhein-Westfalen, the Regierende Bürgermeister von Berlin – Senatskanzlei Wissenschaft und Forschung, and the Bundesministerium für Bildung und Forschung is gratefully acknowledged. I.P. acknowledges support from KAUST (baseline funding BAS/1/1323-01-01).

The authors thank the referees for their valuable comments and suggestions, which helped to greatly improve the presentation quality of this work.

[1] H. G. Tompkins and E. A. Irene, *Handbook of Ellipsometry* (William Andrew, Inc., Norwich, 2005).
[2] H. Fujiwara, *Spectroscopic Ellipsometry: Principles and Applications* (John Wiley & Sons, Ltd, Chichester, 2007).
[3] M. Losurdo and K. Hingerl, *Ellipsometry at the Nanoscale* (Springer Berlin Heidelberg, 2013).
[4] K. Hinrichs and K.-J. Eichhorn, *Ellipsometry of Functional Organic Surfaces and Films* (Springer-Verlag Berlin Heidelberg, 2018).
[5] J. J. Gil Pérez and R. Ossikovski, *Polarized Light and the Mueller Matrix Approach* (CRC Press, 2016).
[6] T. W. H. Oates, T. Shaykhutdinov, T. Wagner, A. Furchner, and K. Hinrichs, "Mid-infrared gyrotropy in split-ring resonators measured by Mueller matrix ellipsometry," Optical Materials Express **4**, 2646–2655 (2014).
[7] F. Carmagnola, J. M. Sanz, and J. M. Saiz, "Development of a Mueller matrix imaging system for detecting objects embedded in turbid media," Journal of Quantitative Spectroscopy and Radiative Transfer **146**, 199–206 (2014).
[8] A. Arwin, A. Mendoza-Galván, R. Magnusson, A. Andersson, J. Landin, K. Järrendahl, E. Garcia-Caurel, and R. Ossikovski, "Structural circular birefringence and dichroism quantified by differential decomposition of spectroscopic transmission Mueller matrices from Cetonia aurata," Optics Letters **41**, 3293–3296 (2016).
[9] W. Li, H. Jiang, C. Zhang, X. Chen, H. Gu, and S. Liu, "Characterization of curved surface layer by Mueller matrix ellipsometry," Journal of Vacuum Science & Technology B **34**, 020602 (2016).
[10] A. Peinado, M. Kildemo, L. M. S. Aas, C. Martella, M. C. Giordano, D. Chiappe, F. Buatier de Mongeot, F. Borondics, and E. Garcia-Caurel, "IR-Mueller matrix ellipsometry of self-assembled nanopatterned gold grid polarizer," Applied Surface Science **421**, 728–737 (2017).
[11] T. A. Germer, "Full four-dimensional and reciprocal Mueller matrix bidirectional reflectance distribution function of sintered polytetrafluoroethylene," Applied Optics **56**, 9333–9340 (2017).
[12] M. Wang, A. Löhle, B. Gompf, M. Dressel, and A. Berrier, "Physical interpretation of Mueller matrix spectra: a versatile method applied to gold gratings," Optics Express **25**, 6983–6996 (2017).
[13] A. T. Martin, S. M. Nichols, M. Tan, and B. Kahr, "Mueller matrix modeling of thick anisotropic crystals with metallic coatings," Applied Surface Science **421**, 578–584 (2017).
[14] B. Song, H. Gu, S. Zhu, H. Jiang, X. Chen, C. Zhang, and S. Liu, "Broadband optical properties of graphene and HOPG investigated by spectroscopic Mueller matrix ellipsometry," Applied Surface Science **439**, 1079–1087 (2018).
[15] A. Mendoza-Galván, L. F. del Río, K. Järrendahl, and H. Arwin, "Graded pitch profile for the helicoidal broadband reflector and left-handed circularly polarizing cuticle of the scarab beetle Chrysina chrysargyrea," Scientific Reports **8**, 6456 (2018).
[16] B. Gompf, M. Gill, M. Dressel, and A. Berrier, "On the depolarization in granular thin films: a Mueller-matrix approach," Optics Express **35**, 301–308 (2018).
[17] A. Furchner, C. Walder, M. Zellmeier, J. Rappich, and K. Hinrichs, "Broadband infrared Mueller-matrix ellipsometry for studies of structured surfaces and thin films," Applied Optics **57**, 7895–7904 (2018).
[18] J.-C. Cigal, *A Novel Spectroscopic Ellipsometer in the Infrared*, Ph.D. thesis, Technische Universiteit Eindhoven, Eindhoven, The Netherlands (2002).
[19] R. A. Chipman, "Polarimetry," in *Handbook of Optics*, edited by M. Bass (McGraw Hill, New York, 1995).
[20] R. M. A. Azzam, I. M. Elminyawi, and A. M. El-Saba, "General analysis and optimization of the four-detector photopolarimeter," Journal of the Optical Society of America A **5**, 681–689 (1988).
[21] D. Layden, M. F. G. Wood, and I. A. Vitkin, "Optimum selection of input polarization states in determining the sample Mueller matrix: a dual photoelastic polarimeter approach," Optics Express **20**, 20466–20481 (2012).
[22] S. R. Cloude, "Conditions For The Physical Realisability Of Matrix Operators In Polarimetry," in *Polarization Considerations for Optical Systems II*, Vol. 1166 (Proceedings of SPIE, 1990) pp. 177–185.
[23] R. Ossikovski, M. Anastasiadou, S. Ben Hatit, E. Garcia-Caurel, and A. De Martino, "Depolarizing Mueller matrices: how to decompose them?" physica status solidi (a) **205**, 7020–727 (2008).
[24] N. B. McKeown and P. M. Budd, "Polymers of intrinsic microporosity (PIMs): organic materials for membrane separations, heterogeneous catalysis and hydrogen storage," Chemical Society Reviews **35**, 675–683 (2006).
[25] W. Ogieglo, A. Furchner, X. Ma, K. Hazazi, A. T. Alhazmi, and I. Pinnau, "Thin Composite Carbon Molecular Sieve Membranes from a Polymer of Intrinsic Microporosity Precursor," ACS Applied Materials & Interfaces **11**, 18770–18781 (2019).
[26] O. Arteaga, "Useful Mueller matrix symmetries for ellipsometry," Thin Solid Films **571**, 584–588 (2014).
[27] G. E. Jellison, Jr. and J. W. McCamy, "Sample depolarization effects from thin films of ZnS and GaAs as measured by spectroscopic ellipsometry," Applied Physics Letters **61**, 512–514 (1992).
[28] H. Hatori, Y. Yamada, M. Shiraishi, M. Yoshihara, and T. Kimura, "The mechanism of polyimide pyrolysis in the early stage," Carbon **34**, 201–208 (1996).
[29] J. N. Barsema, S. D. Klijnstra, J. H. Balster, N. F. A. van der Vegt, G. H. Koops, and M. Wessling, "Intermediate polymer to carbon gas separation membranes based on matrimid PI"," Journal of Membrane Science **238**, 93–102 (2004).
[30] K. Hazazi, X. Ma, Y. Wang, W. Ogieglo, A. Alhazmi, Y. Han, and I. Pinnau, "Ultra-selective carbon molecular sieve membranes for natural gas separations based on a carbon-rich intrinsically microporous polyimide precursor," Hazazi, Khalid **585**, 1–9 (2019).
[31] K. Hinrichs, D. Tsankov, E.-H. Korte, A. Röseler, K. Sahre, and K.-J. Eichhorn, "Comparative Study of an Anisotropic Polymer Layer by Infrared Spectroscopic Techniques," Applied Spectroscopy **56**, 737–743 (2002).
[32] K. Hinrichs, J. Rappich, and T. Shaykhutdinov, "Field manipulation of infrared absorption properties in thin films," Wiley-VCH **Accepted** (2019), 10.1002/pssb.201900490.
[33] N. A. J. M. van Aerle and A. J. W. Tol, "Molecular Orientation in Rubbed Polyimide Alignment Layers Used for Liquid-Crystal Displays," Macromolecules **27**, 6520–6526 (1994).
[34] R. Buchhold, A. Nakladal, U. Büttner, and G. Gerlach, "The metrological behaviour of bimorphic piezoresistive humidity sensors," Measurement Science and Technology **9**, 354–359 (1998).
[35] J. Stöhr and M. G. Samant, "Liquid crystal alignment by rubbed polymer surfaces: a microscopic bond orientation model," Journal of Electron Spectroscopy and Related Phenomena **98–99**, 189–207 (1999).
[36] G. Harsányi, "Polymer films in sensor applications: a review of present uses and future possibilities," Sensor Review **20**, 98–105 (2000).
[37] C. Liu, "Recent developments in polymer MEMS," Advanced Materials **19**, 3783–3790 (2007).
[38] M. Yamahara, M. Nakamura, N. Koide, and T. Sasaki, "Influence of rubbing conditions of polyimide alignment layer on optical anisotropy of immobilized liquid crystal film," Liquid Crystals **34**, 381–381 (2007).
[39] G. D. Hietpas and D. L. Allara, "The molecular structure of poly(biphenyl

dianhydride-p-phenylenediamine) polyimide thin films by infrared spectroscopy: Thickness dependence of structure in the nano- to micrometer range," Journal of Polymer Science: Part B: Polymer Physics **36** (1998).
[40]E. Garcia-Caurel, R. Ossikovski, M. Foldyna, A. Pierangelo, B. Drévillon, and A. De Martino, "Advanced Mueller Ellipsometry Instrumentation and Data Analysis," in *Ellipsometry at the Nanoscale*, edited by M. Losurdo and K. Hingerl (Springer Berlin Heidelberg, 2013).
[41]M. G. Moharam and T. K. Gaylord, "Rigorous coupled-wave analysis of planar-grating diffraction," Journal of the Optical Society of America **71**, 811–818 (1981).
[42]M. G. Moharam and T. K. Gaylord, "Diffraction analysis of dielectric surface-relief gratings," Journal of the Optical Society of America **72**, 1385–1392 (1982).
[43]L. Li, "Symmetries of cross-polarization diffraction coefficients of gratings," Journal of the Optical Society of America A **17**, 881–887 (2000).

Journal of Vacuum Science Technology B

PLEASE CITE THIS ARTICLE AS DOI: 10.1116/1.5129800

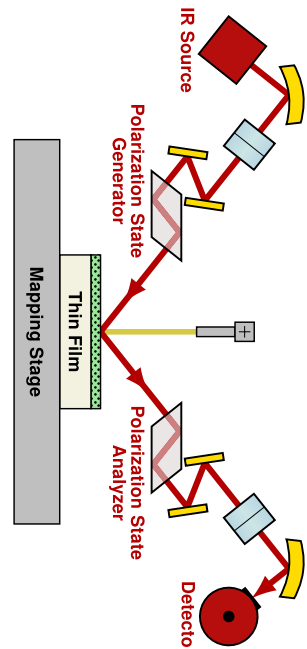

$P = [0°, 90°]$, $A = [0°, 90°]$
W/o Retarders

M_{11}	**M_{12}**	M_{13}	M_{14}
M_{21}	**M_{22}**	M_{23}	M_{24}
M_{31}	M_{32}	M_{33}	M_{34}
M_{41}	M_{42}	M_{43}	M_{44}

$P = [45°, 135°]$, $A = [0°, 90°]$
W/o Retarders

M_{11}	M_{12}	**M_{13}**	M_{14}
M_{21}	M_{22}	**M_{23}**	M_{24}
M_{31}	M_{32}	M_{33}	M_{34}
M_{41}	M_{42}	M_{43}	M_{44}

$P = [45°, 135°]$, $A = [0°, 90°]$
With R_1

M_{11}	M_{12}	M_{13}	**M_{14}**
M_{21}	M_{22}	M_{23}	**M_{24}**
M_{31}	M_{32}	M_{33}	M_{34}
M_{41}	M_{42}	M_{43}	M_{44}

$P = [0°, 90°]$, $A = [45°, 135°]$
W/o Retarders

M_{11}	**M_{12}**	M_{13}	M_{14}
M_{21}	M_{22}	M_{23}	M_{24}
M_{31}	**M_{32}**	M_{33}	M_{34}
M_{41}	M_{42}	M_{43}	M_{44}

$P = [45°, 135°]$, $A = [45°, 135°]$
W/o Retarders

M_{11}	M_{12}	**M_{13}**	M_{14}
M_{21}	M_{22}	M_{23}	M_{24}
M_{31}	M_{32}	**M_{33}**	M_{34}
M_{41}	M_{42}	M_{43}	M_{44}

$P = [45°, 135°]$, $A = [45°, 135°]$
With R_1

M_{11}	M_{12}	M_{13}	**M_{14}**
M_{21}	M_{22}	M_{23}	M_{24}
M_{31}	M_{32}	M_{33}	**M_{34}**
M_{41}	M_{42}	M_{43}	M_{44}

$P = [0°, 90°]$, $A = [45°, 135°]$
With R_2

M_{11}	**M_{12}**	M_{13}	M_{14}
M_{21}	M_{22}	M_{23}	M_{24}
M_{31}	M_{32}	M_{33}	M_{34}
M_{41}	**M_{42}**	M_{43}	M_{44}

$P = [45°, 135°]$, $A = [45°, 135°]$
With R_2

M_{11}	M_{12}	**M_{13}**	M_{14}
M_{21}	M_{22}	M_{23}	M_{24}
M_{31}	M_{32}	M_{33}	M_{34}
M_{41}	M_{42}	**M_{43}**	M_{44}

$P = [45°, 135°]$, $A = [45°, 135°]$
With R_1 and R_2

M_{11}	M_{12}	M_{13}	**M_{14}**
M_{21}	M_{22}	M_{23}	M_{24}
M_{31}	M_{32}	M_{33}	M_{34}
M_{41}	M_{42}	M_{43}	**M_{44}**

Journal of Vacuum Science Technology B

Journal of Vacuum Science Technology B

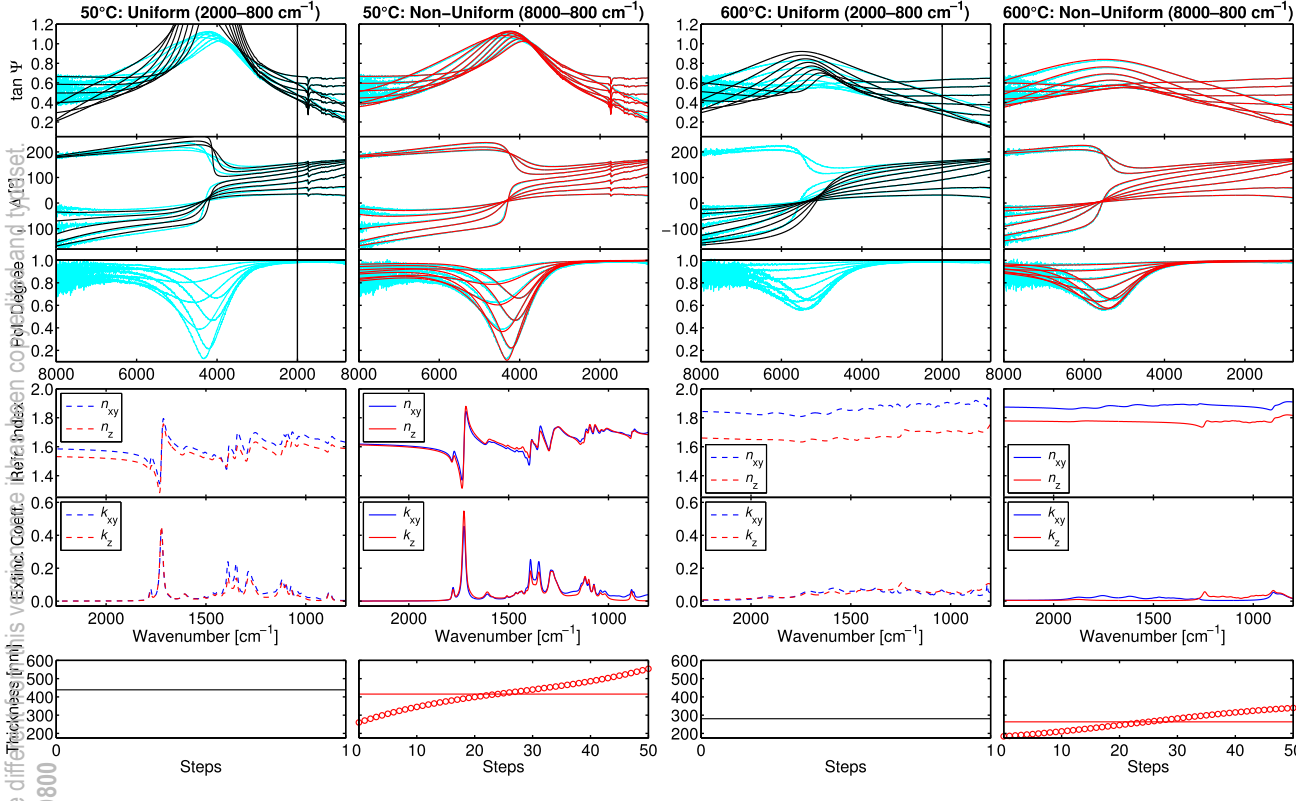

Journal of Vacuum Science Technology B

PLEASE CITE THIS ARTICLE AS DOI: 10.1116/1.5129800

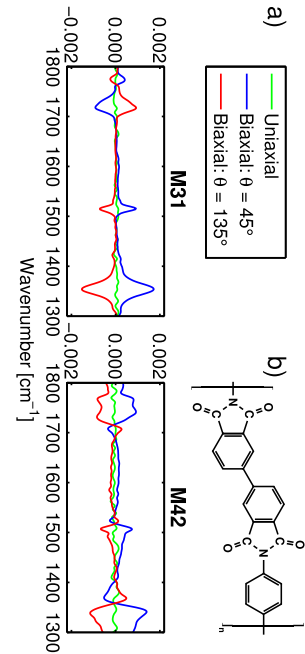

Journal of Vacuum Science Technology B

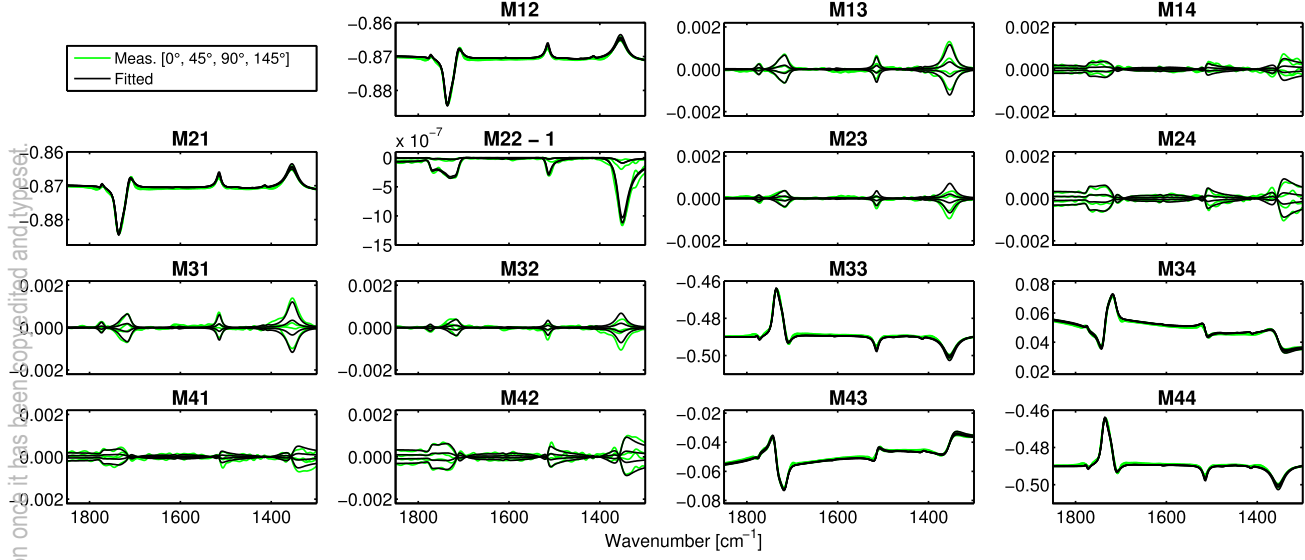

Journal of Vacuum Science Technology B

PLEASE CITE THIS ARTICLE AS DOI: 10.1116/1.5129800

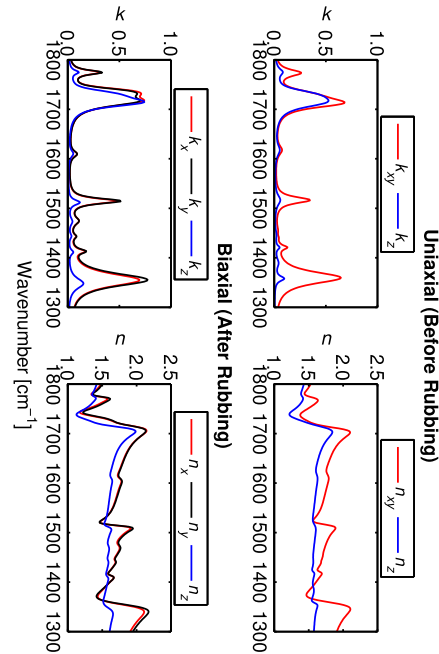

Journal of Vacuum Science Technology B